Appl. Phys. B (2017) 123:160
DOI 10.1007/s00340-017-6733-8

Applied Physics B
Lasers and Optics

Tomographic imaging of reacting flows in 3D by laser absorption spectroscopy

J. Foo[1] · P. A. Martin[1]

Received: 7 February 2017 / Accepted: 13 April 2017 / Published online: 28 April 2017

Abstract This paper describes the development of an infrared laser absorption tomography system for the 3D volumetric imaging of chemical species and temperature in reacting flows. The system is based on high-resolution near-infrared tunable diode laser absorption spectroscopy (TDLAS) for the measurement of water vapour above twin, mixed fuel gas burners arranged with an asymmetrical output. Four parallel laser beams pass through the sample region and are rotated rapidly in a plane to produce a wide range of projection angles. A rotation of 180° with 0.5° sampling was achieved in 3.6 s. The effects of changes to the burner fuel flow were monitored in real time for the 2D distributions. The monitoring plane was then moved vertically relative to the burners enabling a stack of 2D images to be produced which were then interpolated to form a 3D volumetric image of the temperature and water concentrations above the burners. The optical transmission of each beam was rapidly scanned around 1392 nm and the spectrum was fitted to find the integrated absorbance of the water transitions and although several are probed in each scan, two of these transitions possess opposite temperature dependencies. The projections of the integrated absorbances at each angle form the sinogram from which the 2D image of integrated absorbance of each line can be reconstructed by the direct Fourier reconstruction based on the Fourier slice theorem. The ratio of the integrated absorbances of the two lines can then be related to temperature alone in a method termed, two-line thermometry. The 2D temperature distribution obtained was validated for pattern and accuracy by thermocouple measurements. With the reconstructed temperature distribution, the temperature-dependent line strengths could be determined and subsequently the concentration distribution of water across the 2D plane whilst variations in burner condition were carried out. These results show that the measurement system based on TDLAS can be used for 2D temporal or 3D volume imaging of temperature and chemical species concentration in reacting flows.

1 Introduction

The ability to measure non-invasively the spatial distribution of chemical species concentrations and temperature distributions in reacting flows is of importance in a range of application areas but particularly in combustion and plasma science and engineering where it can contribute to designing systems to improve energy efficiency and reduce pollutant species by increased understanding of chemical kinetics, fluid dynamics as well as heat and mass transfer. For practical applications it could be beneficial for the detection of faulty or blocked burners in multi-burner engines such as in some aero-engines. For non-invasive methods, optical diagnostics have been proven to be the most beneficial and these can be categorised as: point measurements, line of sight (LOS) measurements, planar imaging and finally tomographic

This article is part of the topical collection "Field Laser Applications in Industry and Research" guest edited by Francesco D'Amato, Erik Kerstel and Alan Fried.

Electronic supplementary material The online version of this article (doi:10.1007/s00340-017-6733-8) contains supplementary material, which is available to authorized users.

✉ P. A. Martin
philip.martin@manchester.ac.uk

[1] School of Chemical Engineering and Analytical Science, University of Manchester, Sackville Street, Manchester M13 9PL, UK

imaging. Point measurements require successive measurements to build up a volume image. Examples include laser-induced fluorescence (LIF) [1], coherent anti-Stokes Raman spectroscopy (CARS) [2] and two-line atomic fluorescence thermometry (TLAF) [3]. LOS measurements have benefitted from tremendous advances in IR laser absorption spectroscopy with new semiconductor laser sources and many new application areas. An example is tunable diode laser absorption spectroscopy (TDLAS) [4] but more recently quantum cascade lasers have been employed for mid-infrared detection of key chemical species [5]. Cavity-enhanced spectroscopic methods such as cavity-ring down spectroscopy (CRDS) and cavity-enhanced absorption spectroscopy (CEAS) [6] have enabled trace chemical species to be measured.

Planar imaging involves the detection of radiation intensity and has been used to obtain 2D profile information on temperature [7], velocity [8] and mixture fractions [9]. When sequential images are produced in parallel planes then volumetric information can also be extracted [10]. Examples of planar imaging techniques includes Rayleigh scattering [11] and particle imaging velocimetry (PIV) [12]. Planar laser-induced fluorescence (PLIF) [13] uses a laser sheet instead of a beam for measuring 2D species distribution, gas temperature and flow velocity. An example in combustion is the study of water vapour fluorescence at 417 nm that was investigated using two-photon excitation using a KrF laser at 248 nm [14].

Tomographic imaging is not restricted to measuring the distribution of light intensity as in planar imaging. Examples of tomographic studies in combustion science include tomographic X-ray imaging of fuel mass distributions [15] and the use of particle image velocimetry (PIV) for 3D velocity measurements of particles [16]. Tomographic absorption spectroscopy (TAS) uses the absorption or extinction coefficients of absorbing species to reconstruct information on temperature and species concentration [17]. TAS using tunable diode lasers (TDL) has been previously reported for 1D and 2D reconstructions in combustion applications. For example, in-cylinder tomography has been demonstrated by McCann's group with fixed frequency TDL sources [18]. Generally, either direct absorption spectroscopy (DAS) or wavelength modulation spectroscopy (WMS) with tunable diode lasers is proven to be an effective method of signal detection at high molecular specificity with minimal interference from other species [19]. More recently, absorption based non-linear tomography (ABNT) has been proposed which uses widely tunable laser sources such as supercontinuum lasers providing information on several chemical species simultaneously [20]. It has been shown that this approach requires fewer projections to achieve good quality reconstructions so that applications with limited optical access become possible.

There have been limited volumetric or 3D tomographic reconstructions for combustion applications as a function of time using infrared laser absorption tomography therefore the aim of this work was to develop a system for 3D temporal monitoring of temperature and gas concentration of asymmetrical combustion sources using TDLAS. Two-line thermometry was the approach used to extract temperature distributions based on the knowledge of accurate temperature-dependent line strengths over the temperature range expected in combustion applications. Species concentrations can then be extracted from the integrated line absorbance combined with the knowledge of the temperature field and absorption pathlength. In this work, vibration–rotation transitions of water as a product of combustion in the near-infrared spectral region were probed for the temperature distribution and for the determination of water concentration H_2O [19, 21–23].

The paper first describes the background theory of two-line thermometry building our previous work [24] followed by a description of the tomographic reconstruction algorithm used. The experimental setup of the tomography system and reconstruction methodology is described in Sect. 3 followed by the results and discussion on both time-dependent 2D measurements and 3D volumetric measurements in Sect. 4. Finally, Sect. 5 concludes with a discussion of potential improvements.

2 Theoretical background

2.1 Two-line thermometry

The basis of the two-line thermometry technique with tunable laser absorption spectroscopy is the Beer–Lambert law which describes the variation of transmitted light intensity $I(\nu)$ with frequency ν as a monochromatic beam passes through a weakly absorbing medium of length L:

$$\frac{I(\nu)}{I_0(\nu)} = \exp(-\alpha(\nu)L), \tag{1}$$

where $I_0(\nu)$ is the initial light intensity and $\alpha(\nu)$ is the absorption coefficient. The latter can be expressed in terms of the absorption cross section $\sigma(\nu)$ and the number density of absorbing species N:

$$\alpha(\nu) = \sigma(\nu)N. \tag{2}$$

The absorbance is defined as the logarithm of the transmittance in Eq. (1) and then the experimentally measured integrated absorbance A is defined by the area under the absorbance peak:

$$A = \int_{-\infty}^{\infty} \ln \frac{I_0(\nu)}{I(\nu)} \mathrm{d}\nu = \int_{-\infty}^{\infty} \sigma(\nu) NL \mathrm{d}\nu. \quad (3)$$

It is convenient to separate the integrated absorption cross section into an intensity and a line shape term so that the spectral line intensity or line strength S is:

$$S = \int_{-\infty}^{\infty} \sigma(\nu) \mathrm{d}\nu, \quad (4)$$

and the integrated line shape term (or area under the peak), which is often normalised to unity, is given by:

$$\int_{-\infty}^{\infty} g(\nu - \nu_0) \mathrm{d}\nu = 1, \quad (5)$$

where ν_0 is the absorption line centre. Typical units for infrared measurements using wavenumbers (cm^{-1}) are L (cm), N (molecule cm^{-3}), $\sigma(\nu)$ (cm^2 $\mathrm{molecule}^{-1}$), $\alpha(\nu)$ (cm^{-1}), g (cm) and S [cm^{-1}/(molecule cm^{-2})] or (cm $\mathrm{molecule}^{-1}$). The integrated absorbance in terms of line strength is then given by:

$$A = \int_{-\infty}^{\infty} \ln \frac{I_0(\nu)}{I(\nu)} \mathrm{d}\nu = S(T) NL. \quad (6)$$

The temperature dependence of the light transmission is contained in the line strength term $S(T)$ and for a reference temperature of 296 K this is given by

$$S(T) = S(296) \frac{Q(296)}{Q(T)} \exp\left[-\frac{hcE''}{k}\left(\frac{1}{T} - \frac{1}{296}\right)\right] \frac{\left[1 - \exp\left(-\frac{hc\nu}{kT}\right)\right]}{\left[1 - \exp\left(-\frac{hc\nu}{k296}\right)\right]}, \quad (7)$$

where $Q(T)$ is the partition function of the absorbing molecule at temperature T, E'' (cm^{-1}) is the lower state energy level of the transition, h is Planck's constant (J s), c is the speed of light (cm s^{-1}) and k is Boltzmann's constant (J K^{-1}). For two absorption lines 1 and 2, the ratio R of their integrated absorbances is:

$$R = \frac{A_1}{A_2} = \frac{S_1(T)}{S_2(T)} = \frac{S_1(296)}{S_2(296)} \exp\left[-\frac{hc}{k}\left(E_1'' - E_2''\right)\left(\frac{1}{T} - \frac{1}{296}\right)\right]. \quad (8)$$

So if the integrated absorbances of two known absorption lines are measured, then the temperature can be determined if the line strengths are known at a reference temperature and the difference in lower state energies are known:

$$T = \frac{\left(\frac{hc}{k}\right)\left(E_2'' - E_1''\right)}{\ln\left(\frac{A_1}{A_2}\right) + \ln\left(\frac{S_2(296)}{S_1(296)}\right) + \left(\frac{hc}{k}\right)\left(\frac{E_2'' - E_1''}{T_0}\right)}. \quad (9)$$

These are often tabulated in databases such as HITRAN [25]. This has been described previously in several papers [24]. When the temperature is determined then the line strength $S(T)$ can be calculated from (7) and the number density N or concentration by the rearrangement of (6).

The sensitivity or precision of the temperature determination is very much dependent on $\mathrm{d}R/\mathrm{d}T$ and the ability to accurately measure the ratio R. Selection of appropriate line pairs is therefore a critical part of the process and different pairs will be required depending on the temperature range of interest. For the precise measurement of integrated absorbance, it is important to have well isolated absorption lines without any spectral interferences and with good signal to noise ratios (large S) but without being optically thick. It is also beneficial to measure both lines on the same sweep of the laser wavelength so that instrumental effects can be ratioed out. For some lasers such as DFB diode lasers used here, the spectral region accessible in a single current scan is often only a few cm^{-1} [26].

Water is commonly used as a probe molecule for two-line thermometry as there are a vast number of absorption lines across the infrared spectrum. The combination band $\nu_1 + \nu_3$ and overtone bands $2\nu_1$ and $2\nu_3$ are used in this work [19, 21–23, 27].

The above discussion refers to a homogeneous or uniform distribution of absorbers and temperature. For a non-uniform distribution along the laser beam path l, the integrated absorbance for the ith transition is given by

$$A_i = \int_0^L N(x_l, y_l) S_i\left[T(x_l, y_l)\right] \mathrm{d}l, \quad (10)$$

where $N(x_l, y_l)$ is the number density at the coordinates (x_l, y_l) probed by the laser beam and $S_i[T(x_l, y_l)]$ is the line strength of the ith transition at temperature T on the x, y grid. The pressure is assumed constant. The aim is to reconstruct $T(x, y)$ followed by $N(x, y)$ using a tomographic reconstruction algorithm.

2.2 Reconstruction algorithms

The optical plane where the measured objects are located is termed as the space domain and is a two-dimensional function, $f(x, y)$. In this work the image to be reconstructed is based on the spatial variation of absorption coefficient at each optical frequency of the laser $\alpha_\nu(x, y)$ from which the image of the integrated absorbance $A_i(x, y)$ can be determined for each absorption transition, i. Several parallel beams probe the sample to produce projections of absorption coefficient at different angles, θ. The beams or line integrals shown in Fig. 1 are defined by a unique equation based on the angle (θ) in relation to the sample object as

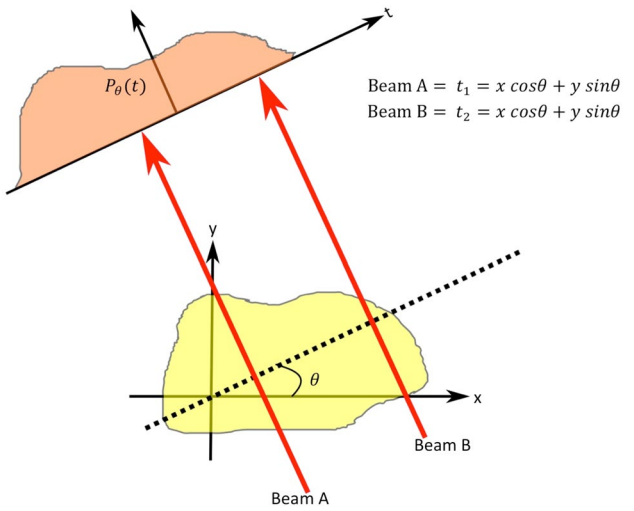

Fig. 1 Example of object in 2D function (x, y) with individual line integrals forming a Radon Transform

well as its coordinates as shown in (11). These line integrals are also represented as functions of (θ, t) [28]:

$$x\cos\theta + y\sin\theta = t. \tag{11}$$

A combination of laser beams or line integrals from t_1 to t_n at a set angle θ_i will form a singular parallel projection represented by $P_\theta(t)$ in Fig. 1, where t is the location of the line integral along an arbitrary line on θ [28].

The function $P_\theta(t)$, also known as the Radon transform of the measured optical plane $f(x, y)$ can be expressed in (12), where l specifies an integration path [28].

$$P_\theta(t) = \int_{(\theta,t)\text{line}} f(x,y)\mathrm{d}l. \tag{12}$$

$P_\theta(t)$ is two dimensional making up all the projection slices at different angles θ into a 2D format called the sinogram. There are then two distinct approaches to carrying out the inversion to obtain $f(x, y)$ from $P_\theta(t)$, these are transform-based or analytical approaches such as filtered back-projection (FBP) or algebraic iterative methods such as the algebraic reconstruction technique (ART) used in our previous work [24]. In this work we use the analytical transform-based approach because it is better suited to parallel beam sampling with unrestricted optical access to the object. This approach is also generally used for X-ray tomography such as in CT scans [28].

The cornerstone of the transform-based approach is the Fourier slice theorem (FST) or central slice theorem (CST) [28]. This states that the Fourier transform of a projection at a specific angle is equivalent to one slice of the 2D Fourier transform of the object at that angle. Figure 2 depicts the use of the FST to transform information from the space domain into the frequency domain. The FST is executed by performing a 1D Fourier transform of a parallel projection and by allocating it to a 2D Fourier transform of the original optical plane measurement area. Projections at multiple angles will therefore populate the frequency domain and it should then be possible to obtain the original function by a 2D inverse Fourier transform.

The 2D transform F of the object function $f(x, y)$ is given in (13), where u and v are the axes in the frequency domain [28].

$$F(u,v) = \int_{-\infty}^{\infty}\int_{-\infty}^{\infty} f(x,y)\mathrm{e}^{-j2\pi(ux+vy)}\mathrm{d}x\mathrm{d}y. \tag{13}$$

The Fourier transform of the projection at each angle, $P_\theta(t)$, can be likewise given by:

$$S_\theta(w) = \int_{-\infty}^{\infty} P_\theta(t)\mathrm{e}^{-j2\pi wt}\mathrm{d}t. \tag{14}$$

As there are only a limited number of projections in practice, the function $F(u, v)$ is only known along a finite number of radial lines in frequency space. In order that the inverse 2D Fourier transform can be applied, it is necessary to interpolate from these radial points onto a Cartesian grid. However, there are fewer radial points further away from the centre of the grid making the interpolation error larger and leading to a greater error in the high frequency components and image degradation (blurring). This can be mitigated by multiplication with a 2D ramp filter before the inverse 2D Fourier transform step. The object image is therefore given by:

$$f(x,y) = \int_0^{\pi}\left[\int_{-\infty}^{\infty} S_\theta(w)|w|\mathrm{e}^{j2\pi wt}\mathrm{d}w\right]\mathrm{d}\theta, \tag{15}$$

where the frequency response of the filter is given by $|w|$ giving rise to the term 'filtered projection' [28]. This procedure is carried out for the two sinograms produced by integrated absorbances of the two absorption lines to produce $A_1(x, y)$ and $A_2(x, y)$ from which the temperature distribution $T(x, y)$ and chemical species concentration distribution $N(x, y)$ can be determined.

2.3 Computer implementation

The Fourier transform can be implemented with a FFT (fast Fourier transform) algorithm, by bandlimiting the Fourier transformed slices. A band-limited Fourier transform assumes components over a certain frequency to be negligible (zero) and suitable for an FFT algorithm to be a good approximate to the Fourier transform in (14). Filters are used to suppress high frequencies, which tend to be caused by observation noise. These filters are usually convoluted to the projection slices, either in the spatial domain or in the frequency domain. Zero padding consists of adding a trail of zeros to the projection slices and this will decrease

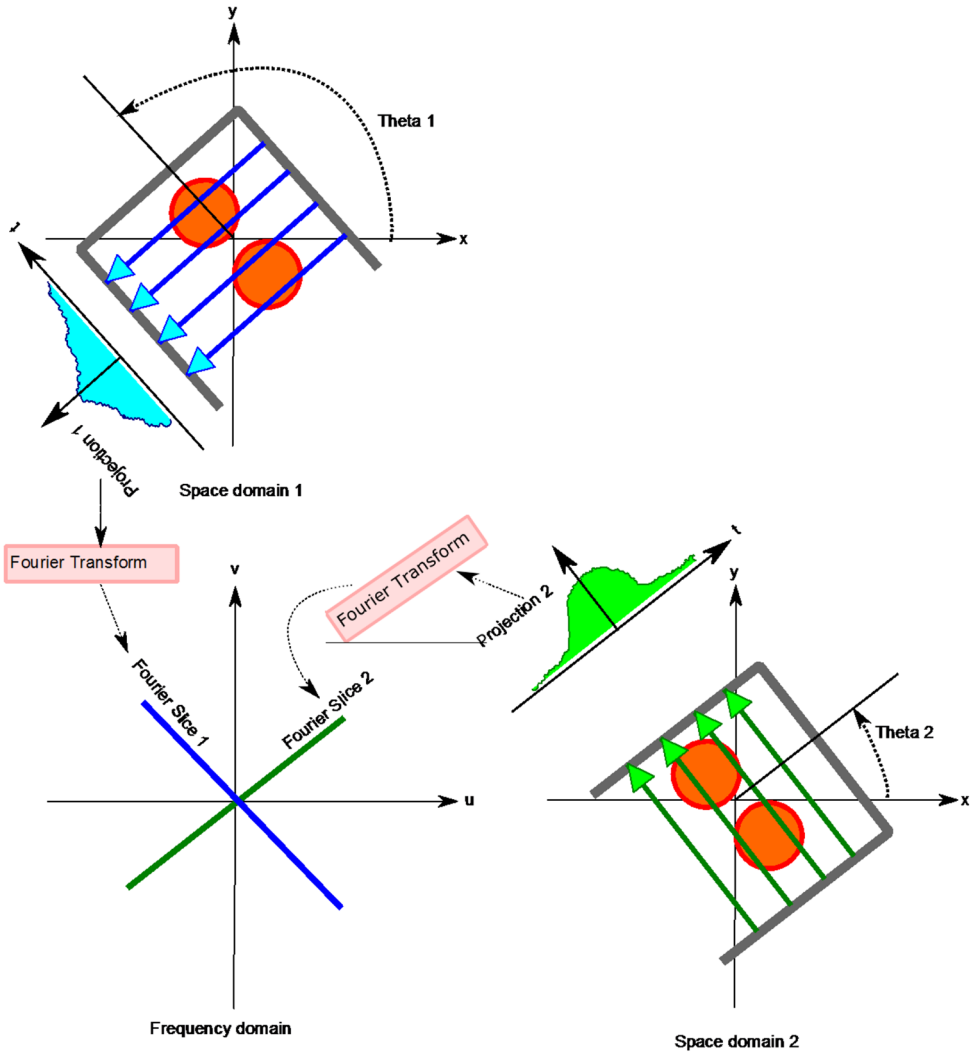

Fig. 2 The translation of projection slices from the space domain to the frequency domain Fourier slices via Fourier transform

the step size/cell size of the data points in the Fourier domain. Adequate zero padding reduces the overall formation of artefacts caused by inter-period interference present in the reconstruction images by producing smoother individual spectra.

3 Experimental

3.1 Design and construction of 3D tomography system

The 3D tomography system is shown in Fig. 3 and comprised three main components: the external frame, the rotator and the burner carrier, each defined by its own cage. The external frame which housed the two 'cages' was the largest, and with dimensions of 90 cm width by 90 cm depth by 100 cm height. A 90-cm-long central bar supported by two rails of 40 cm high further extended the height. The external frame sat on four legs of 10 cm each. The rotator sat in the bottom half of the external frame with dimensions of 37 cm width by 37 cm depth by 60 cm height. Finally the burner carrier, which was the smallest 'cage', had the dimensions of 22 cm width by 22 cm depth by 28 cm height. The external frame also acted as a barrier to protect users from accidentally touching the moving components or heat source during operation.

The rotator held the moving cage, which was located inside the bottom half of the external frame. It was placed on a 38-cm diameter circular bearing, which was made up of a stationary half and a rotating half. This circular bearing also had a hollow inner hole of diameter 28 cm as shown in Fig. 3. The stationary half of the bearing was mounted to the bottom of the external frame to secure the bearing to a stationary object whilst the rotator was screwed onto the rotating other half of the bearing. The rotating half was connected to a 6 V motor (SpringRC Sm-S4303R) located at the bottom of the circular bearing and fixed onto the external frame. This motor was

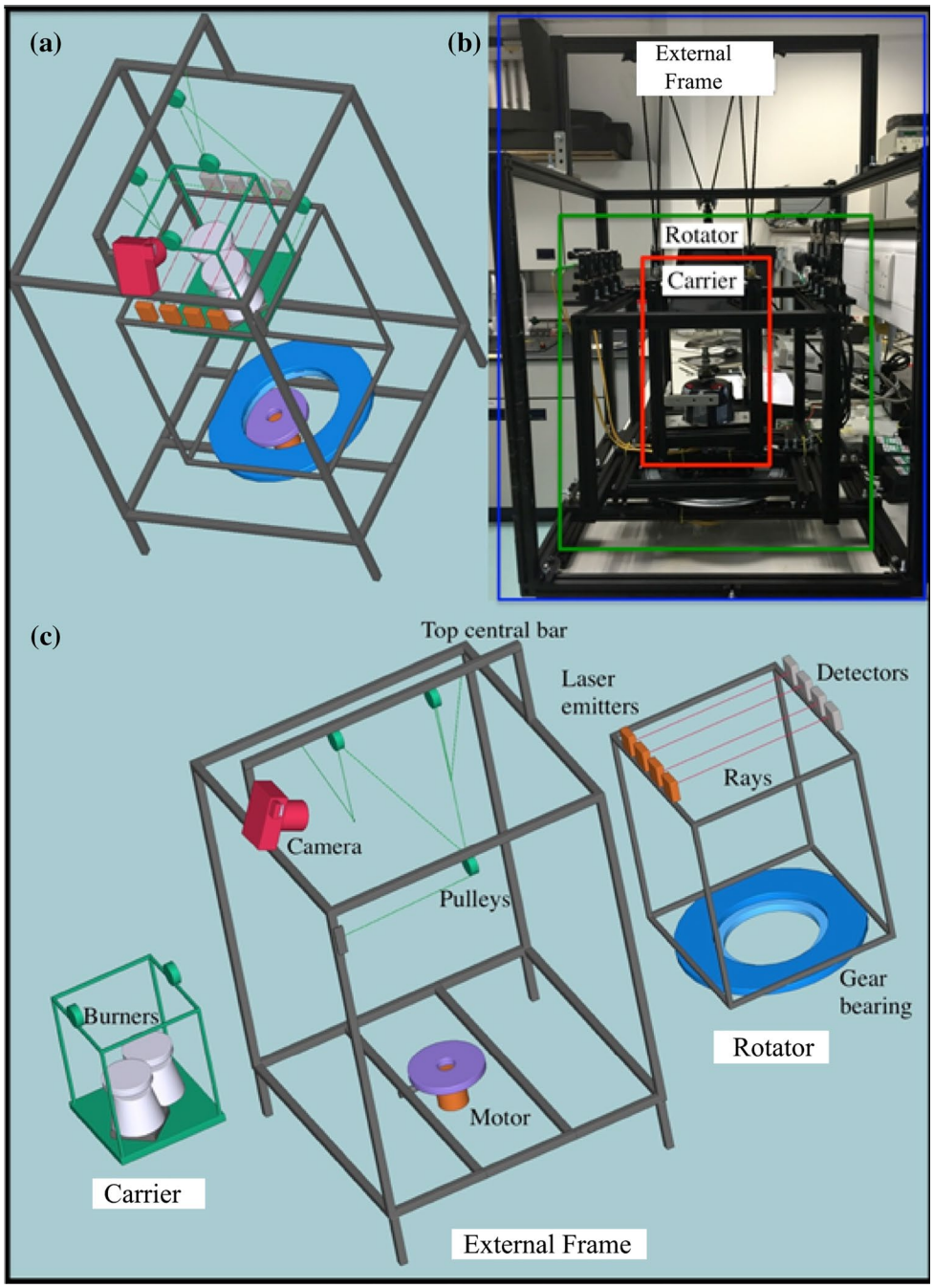

Fig. 3 **a** Overall view of the full setup from the *top*. **b** The corresponding photo of the setup, with each primary section *boxed* out in *blue* (external frame), *green* (rotator) and *red* (carrier). **c** Exploded view of the setup, with each primary section removed for a clearer view of the individual segments

connected via a cable to a printed circuit board (PCB) (Phidgets AdvanceServo-1061), which was controlled directly from the laptop via LabVIEW. The motor with no load had a technical specified maximum rotational speed of 54 rpm. However, the motor behaved differently under additional load from the rotator. With this current setup, the maximum rotation speed was 16.6 rpm, and the slowest speed was 5.7 rpm. This was calculated from the fastest speed per single rotation during the experiment to be at 1.8 s and the slowest speed to be at 5.2 s (lowest speed possible to break inertia from weight). The final cage is the burner carrier. This is the cage that holds the burners that are lowered into the rotator. It was fitted with two 3-cm diameter pulleys on the top. Two similar pulleys were also installed below the external frame central bar. Each of the individual pulleys on the carrier was connected to the external frame central pulley with their individual rope. A final similar pulley was installed in the middle of the external frame front where both ropes were fed to ensure equal force during height adjustment.

A camera (Olympus E-P2 with a 14–42 mm zoom lens) was also attached to the central bar of the external frame to record throughout the course of the experiments.

In order to prevent cable tangling the rotator platform only rotated 180° before returning back to the starting position. A program written using LabVIEW 2010 was used to control the laser and motor, as well as to receive the attenuated laser signals from the detector. The detector received signals at a rate of 10 ms per spectrum. However, the rotator does not stop for data acquisition at each projection angle, which means that the recorded spectrum is actually not at a single projection angle, but at a small range of projection angles. The range of projection angle depends both on acquisition rate, as well as the speed of rotation. Assuming that the acquisition rate is fixed at 10 ms/av. spectrum, then the faster the speed of rotation and the larger the range of projection angle, $\Delta\theta°$. The minimum time duration for the collection of spectra for a 2D tomographic image was 1.8 s corresponding to $\Delta\theta° = 1°$ whereas the slower speed of 5.7 rpm corresponds to $\Delta\theta° = 0.34°$. As shown in Sect. 5.2 later a compromise of speed and spatial resolution of 360 projections over 180° with $\Delta\theta° = 0.5°$ was used for the measurements described here.

3.1.1 Burners

Each burner had jets around the circumference of the flat 9 cm diameter head and the isobutane/propane fuel mix was controlled by a valve on top of the mixed fuel canister (Jetpower Isobutane/Propane fuel mix 100 g). The total height of the burner, inclusive of the fuel canister, was 11 cm. The exact composition of the mixed fuel was unknown, but it is typical for these types of fuel canister to be approximately 20–30% weight propane and the remainder to be isobutane. A non-symmetrical flame distribution for each burner was achieved by covering half the jets with aluminium foil (as shown in Fig. 15 in Sect. 3.5). Two adjacent burners with the jets partially covered with metal foil were used during the experiments, resulting in two asymmetrical shapes. The burners were adjusted manually in quick succession during the temporal experiments. To ensure that the burner was operating in steady state after each adjustment and before the next sequential image acquisition, a high frame rate video capture camera was used. The camera used was a 12 MP GoPro HERO4, recording video at 32 frames per second.

To enable 3D volumetric studies of the flames, the position of the optical plane was adjusted by moving the burner carrier instead of the optical plane by means of a pulley system (shown in Fig. 3).

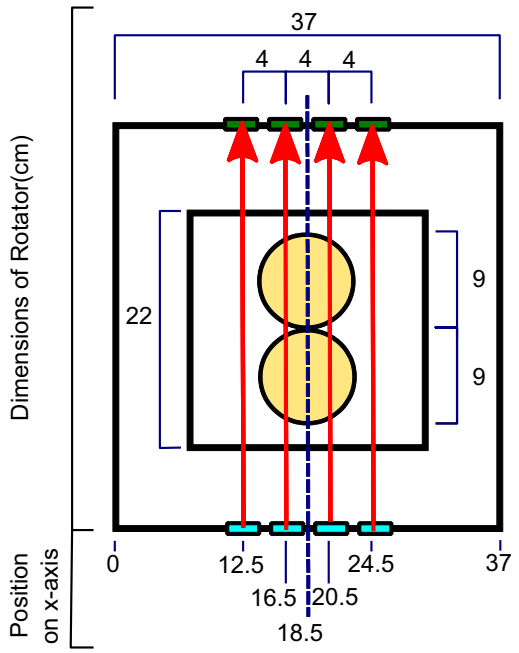

Fig. 4 Schematic showing the dimensions of the experimental setup (cm). The rotator is pictured as the outer *black square* while the carrier is pictured as the inner *black square*. The layout of laser source emitters (*cyan rectangles*) and photo detectors (*green rectangles*) are shown on the rotator. Four laser beams are shown as *red*. Two *yellow* discs representing the burners are located in the centre of the carrier. The layout is depicted at $\theta = 0°$. The locations of the laser source emitters and rotator mid-point are located in the *bottom* of the figure in cm. The mid-point of the rotator is 18.5 cm

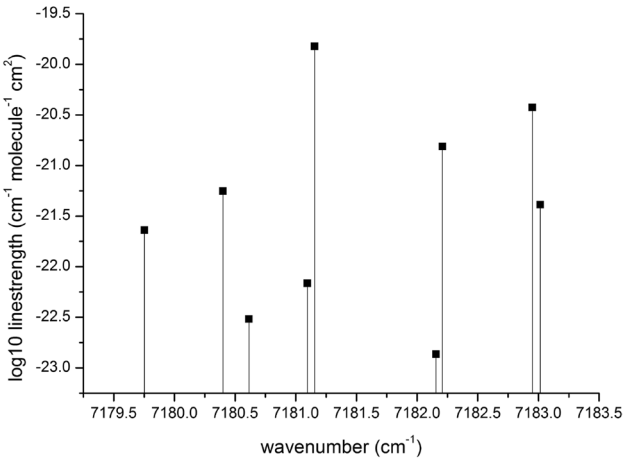

Fig. 5 Line strengths above 10^{-23} cm^{-1} $molecule^{-1}$ cm^2 used in the peak fitting process. Extracted from HITRAN 2008 at 296 K [29]

3.2 Line selection

The spectral region probed for water transitions was around 7179–7183 cm^{-1} (Fig. 4). A stick plot showing the line strengths at 296 K of the measured transitions is shown in

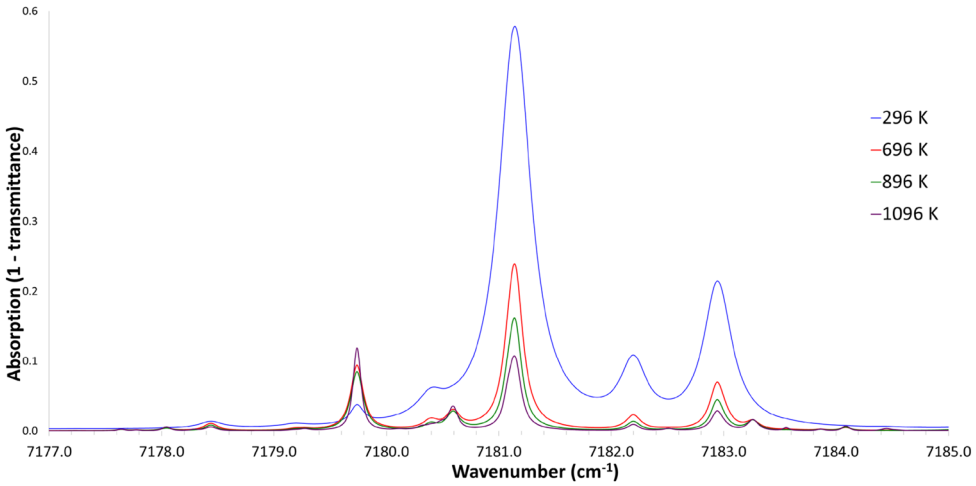

Fig. 6 Simulation of the temperature dependence of the near-infrared spectrum of water around 7180 cm^{-1} or 1392.7 nm between 296 and 1096 K. This was simulated using the spectral simulator Spectralcalc (http://www.spectralcalc.com) (using HITRAN 2008 [29]) for an H_2O mixing ratio of 0.1 in air, a pressure of 1013.25 mbar and an absorption path length of 10 cm

Fig. 5. Figure 6 shows a simulated absorption spectral plot of this region for a temperature range from 296 to 1096 K for a pressure of 1013.25 mbar, an absorption pathlength of 10 cm and an H_2O mixing ratio of 0.1 in air. Most of the absorption features reduce in intensity as the temperature increases such as the intense line at 7181.156 cm^{-1} (line 1). However, there is a line at 7179.752 cm^{-1} (line 2) which shows the opposite temperature dependence with the intensity increasing with temperature. Figure 7 shows this more clearly for the temperature dependence of these two lines along with the ratio, R (given by (8)). The temperature dependence of R was then used in the reconstruction of temperature and water concentration. The tabulated data for the measured lines from the HITRAN 2008 database [29] are given in Table 1.

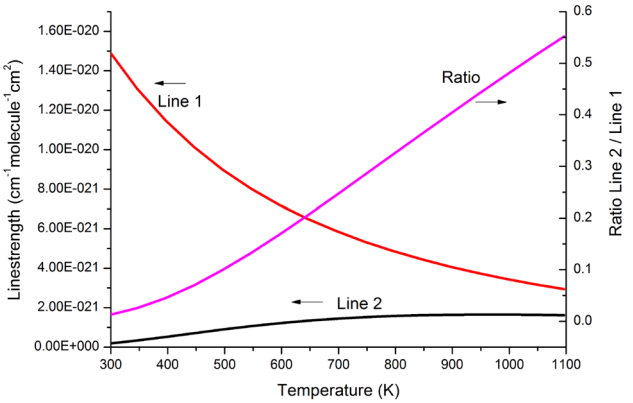

Fig. 7 Variation of line strength (*left vertical axis*) of the transitions at 7179.752 cm^{-1} (line 2, *black*) and 7181.156 cm^{-1} (line 1, *red*) with temperature. The ratio of the two line strengths as a function of temperature is shown in *magenta* (*right vertical axis*). This ratio, R, is given by (8)

3.3 Laser absorption spectroscopy setup with four channels

The laser was a pig-tailed distributed feedback (DFB) diode laser in a butterfly mount (Thorlabs LM14S2) and centred around 7178 cm^{-1} (1392 nm) with a maximum output power of 10 mW (Eblana Photonics EP1392-DM-B01-FA). The laser temperature was controlled by a temperature controller (Thorlabs TED 200C) and the current ramp was controlled by the laser current controller (Thorlabs LDC 205C). These in turn were controlled by a LabView program (National Instruments) on a laptop computer with an 18-bit data acquisition board (DAQ) (National Instruments NI-USB 6281) with an aggregate maximum sampling rate of 500 kS s^{-1}. By a combination of temperature and current adjustments the laser output ranged from 7155 to 7185 cm^{-1}. The output of the laser diode was divided by a 1 × 4 fibre splitter (Topfibre tech S/N AA002048) and the four single mode fibres were fed through the bottom of the external frame through the central hole within the circular bearing and the bottom of the rotator and finally mounted on top of the rotator. Collimating lenses (ThorLabs F230SMA-C) were used to collimate the laser beams to a diameter of approximately 1.5 mm over a path length of 37 cm. The emitters were centred in the middle of the rotator and placed 4 cm apart as shown in Fig. 4.

Four InGaAs switchable-gain photo detectors (Thorlabs PDA10CS-CS) with 2 mm diameter active area were mounted 4 cm apart from each other on the rotator opposite the laser transmitters as shown in Fig. 4.

The wired electrical and data cables were also similarly fed through under the external frame, through both the circular bearing and the bottom of the rotator. The detectors received the attenuated signals from the lasers and feed the data back to the DAQ and then recorded in the computer via LabView. The data of each

Table 1 Line data from HITRAN 2008 [29]

Line	Line centre, ν_0 (cm^{-1})	Line strength, S (molecule cm^{-1}) at 296 K	Einstein A-coefficient, A ($Debye^2$)	Air broadened half-width (cm^{-1} atm^{-1})	Self-broadened half-width (cm^{-1} atm^{-1})	Lower energy level E'' (cm^{-1})
1	7179.752	2.30E−22	12.83	0.0456	0.265	1216.195
2	7180.400	5.61E−22	0.5419	0.098	0.500	224.838
3	7180.613	3.04E−23	4.764	0.0582	0.295	1477.297
4	7181.095	6.86E−23	3.829	0.0442	0.384	1216.195
5	7181.156	1.51E−20	13.27	0.0997	0.488	136.762
6	7182.156	1.37E−23	0.01816	0.0894	0.439	382.517
7	7182.209	1.54E−21	1.432	0.107	0.375	42.372
8	7182.950	3.75E−21	10.2	0.097	0.51	142.278
9	7183.016	4.12E−22	0.3598	0.101	0.492	134.902

detector channel were received by the DAQ simultaneously through multiple analogue channels on the DAQ.

3.3.1 Waveform modulation, peak selection and analysis

A single cycle of wavelength tuning consists of ramping the laser current linearly for the first 1.6 ms in order to tune through the water absorption profiles. The current is then dropped below the lasing threshold for the next 0.4 ms in order to measure the background baseline. This is repeated 5 times producing a total of 1000 data points per single cycle. The 5 wavelength scans within the cycle are then averaged to form a spectrum of 200 data points in 10 ms enabling 100 spectra to be acquired per 1 s. The rate of photodetector data acquisition was set at a maximum frequency of 100 kHz. Each of the four channels was read in parallel. The fastest acquisition enabled a rotation of 0° to 179° to be scanned in 1.8 s (Fig. 8).

The scale was converted from data points (or scan time) to relative wavenumber using a Fabry–Perot etalon. The transmission signal $I(\nu)$ was fitted to a function comprising a Lorentzian line shape function for each of the nine absorption lines (see Table 1) combined with a third-order polynomial to describe the varying background intensity produced by the laser current ramp:

$$I(\nu) = \left(I_0 + I_1\nu + I_2\nu^2 + I_3\nu^3\right) \times \exp\left(-\sum_{i=1}^{9} 2A_i w_i \Big/ \left(\pi\left(w_i^2 + 4(\nu - \nu_{0i})^2\right)\right)\right), \tag{16}$$

where ν_0 is the line centre of the ith line, w_i is the full width at half maximum (FWHM) and A_i is the area of the peak or integrated absorbance. Non-linear least squares fit to the transmission spectrum using initial parameters from the previous fit. As the temperature was unknown then the A_i values were all floated within each fit subject to constraints such as ν_{0i} and w_i as well as no negative values. The effect of temperature on the line widths would have the effect of producing small errors due to fixing the widths during the fitting process. Figure 9 shows the results of the fitting process including the observed minus calculated residual. The integrated absorbances for the two selected lines (7181.156 cm^{-1} line 1 and 7179.752 cm^{-1} line 2) were then saved and used to form the sinogram.

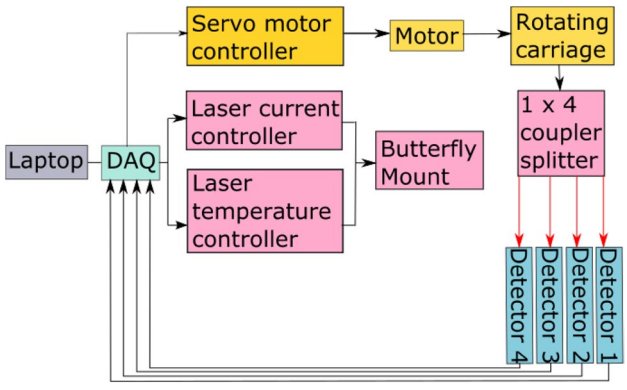

Fig. 8 Schematic layout of the experimental set-up and control system

3.4 Tomographic reconstruction

The reconstruction program was written in MATLAB 2013 [30] and works by separately analysing the integrated absorbance (A_1 and A_2) of each of the two selected absorption lines for each projection and then reconstructing the spatial distribution of each integrated absorbance. Values in the two grids were then ratioed to extract the temperature distribution following the two-line thermometry approach (Sect. 2.1) followed by extraction of the water concentration distribution from the temperature-dependent line strengths.

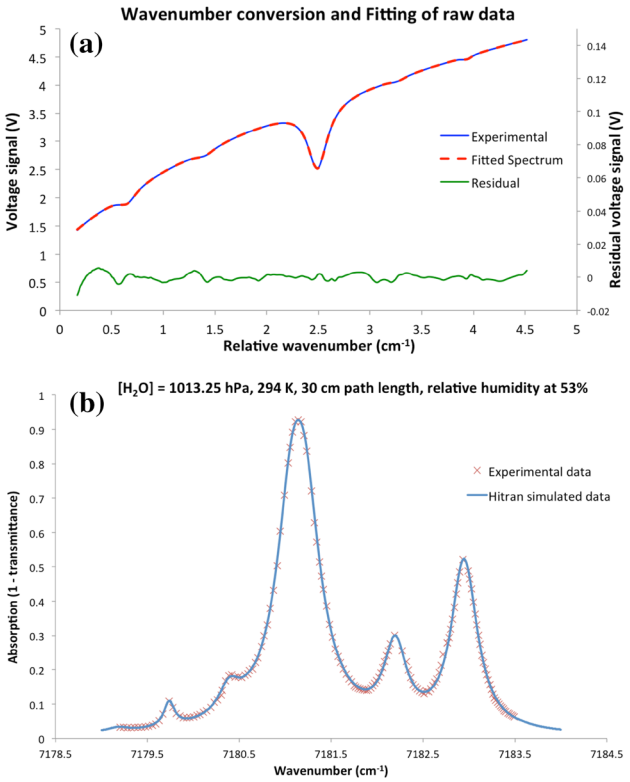

Fig. 9 **a** Fitting of a sample spectrum after wavenumber conversion. The experimental spectrum is in *blue*, with the peak fitting in *red dashes* (both *left vertical axis*). The residual is in *green* (*right vertical axis*). **b** Laser operating at 15 °C wavenumber sweep from 7179.2 to 7183.4 cm^{-1} in comparison to HITRAN 2008 data [29] simulated at same experimental conditions. Simulation data obtained from http://www.spectralcalc.com

From the experiment, there were four pairs of integrated absorbance values per projection angle. The 4 cm separation of each measurement channel was considered sparsely populated as the objects scanned were only 9–18 cm. Linear interpolation was therefore carried out from 4 to 37 data points on a cm scaled grid to match the length of the rotator cage. Values (integrated absorbance values) outside the four original data points were interpolated towards values measured at room conditions and not influenced by the operation of the burners prior to the start of each experiment. This was verified by thermocouple measurements. These interpolated projection slices from each projection angle from 0 to 179° with a step size of 0.5° were used to build the two sinograms to be used in the reconstruction. These are illustrated in Figs. 10 and 11.

Each of the sinograms was zero padded (up to 700) in order to produce a smoother final image by decreasing the frequency intervals and thus improving the interpolated Fourier transform. These Fourier transformed, zero padded slices were then transformed onto the Fourier domain grids based on their angle of projection i.e. in polar coordinates. As the initial data sampling or the original sinogram is of a consistent length, the allocation of the Fourier transformed slices that were centred in the middle of the grid of the frequency domain grids form a circular data pattern on a square grid. This was then converted to a Cartesian Fourier space (using the MATLAB function POL2CART). The Cartesian Fourier space was linearly interpolated to smooth the data as shown in Fig. 12. Filtering was then carried out in the frequency domain with a 2D ramp filter. This was

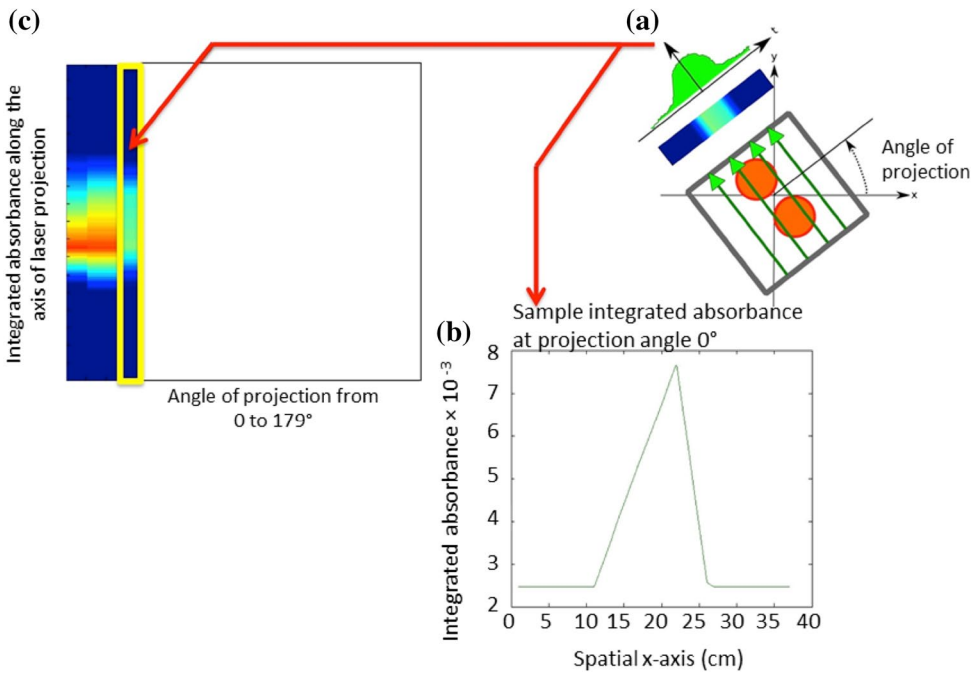

Fig. 10 **a** A sample image of collected integrated absorbance through the laser beams along the angle of projection. **b** Compiled integrated absorbance along the angle of projection. **c** A compiled sinogram of each projection slice (Radon slice) at each projection angle of sampling

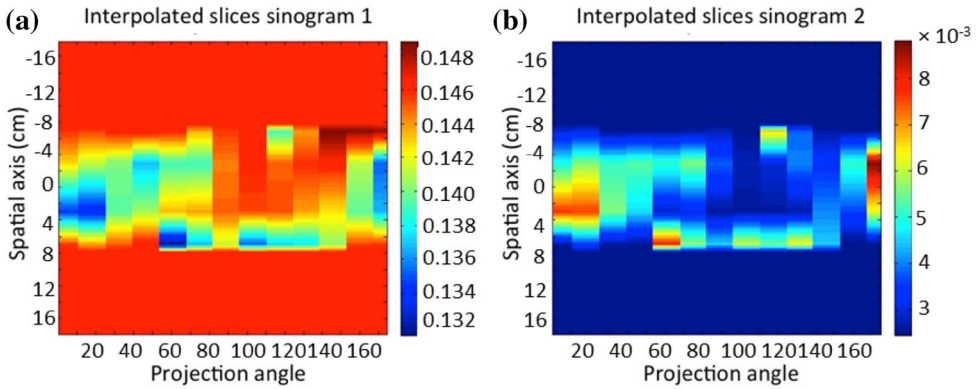

Fig. 11 Sample sinograms of **a** line 1 and **b** line 2. Line 1 corresponds to 7181.156 cm^{-1} and line 2 corresponds to 7179.752 cm^{-1}

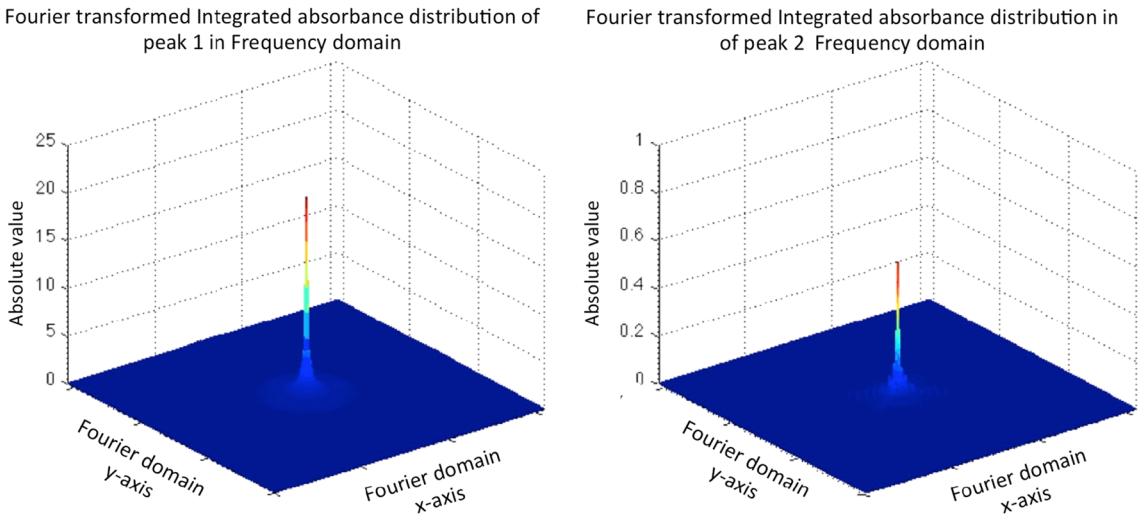

Fig. 12 Allocated Fourier slices interpolated into the frequency domain of peaks (lines) 1 and 2

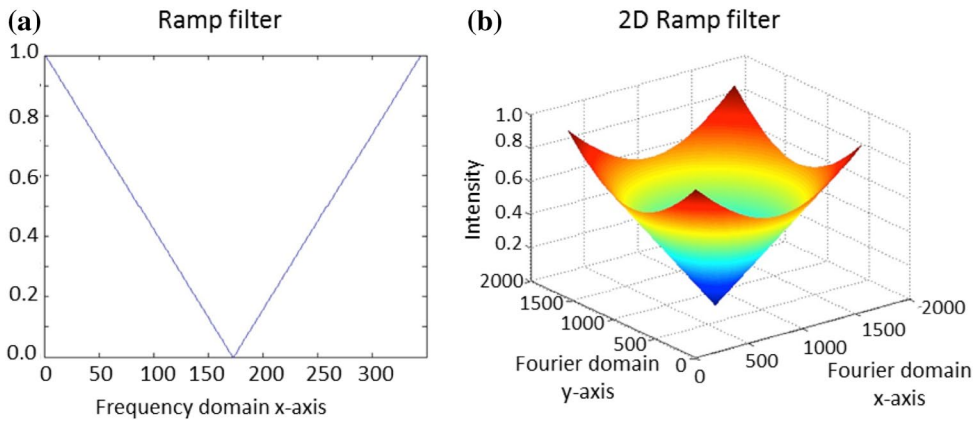

Fig. 13 Conversion from **a** a 1D ramp filter to **b** a 2D ramp filter

generated in a similar way by transforming the ramp filter into the frequency domain grid. See Fig. 13.

The inverse 2D FFT (MATLAB function IFFT2) was then implemented to convert the frequency domain grid back to the two spatial domain grids of integrated absorbance distribution. After cropping, the values in the two grids were divided to produce a single grid containing the ratio of integrated absorbances at each point from which

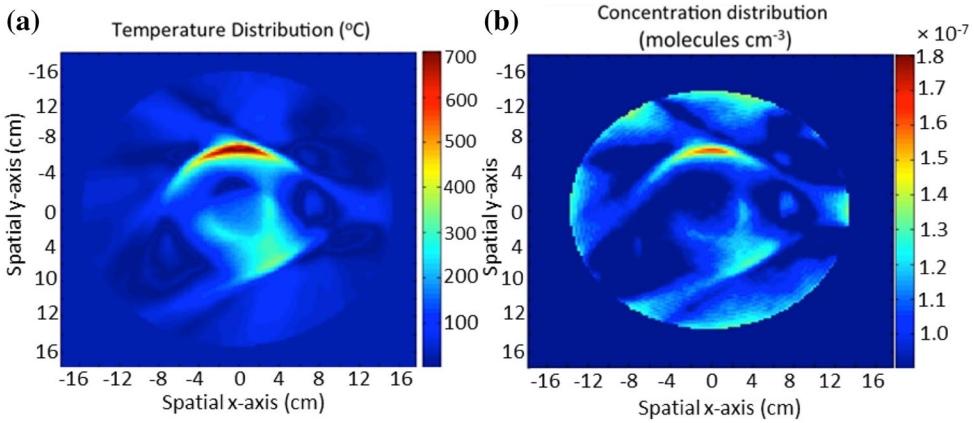

Fig. 14 **a** Temperature and **b** concentration distribution sample images reconstructed by the direct Fourier reconstruction (DFR) method

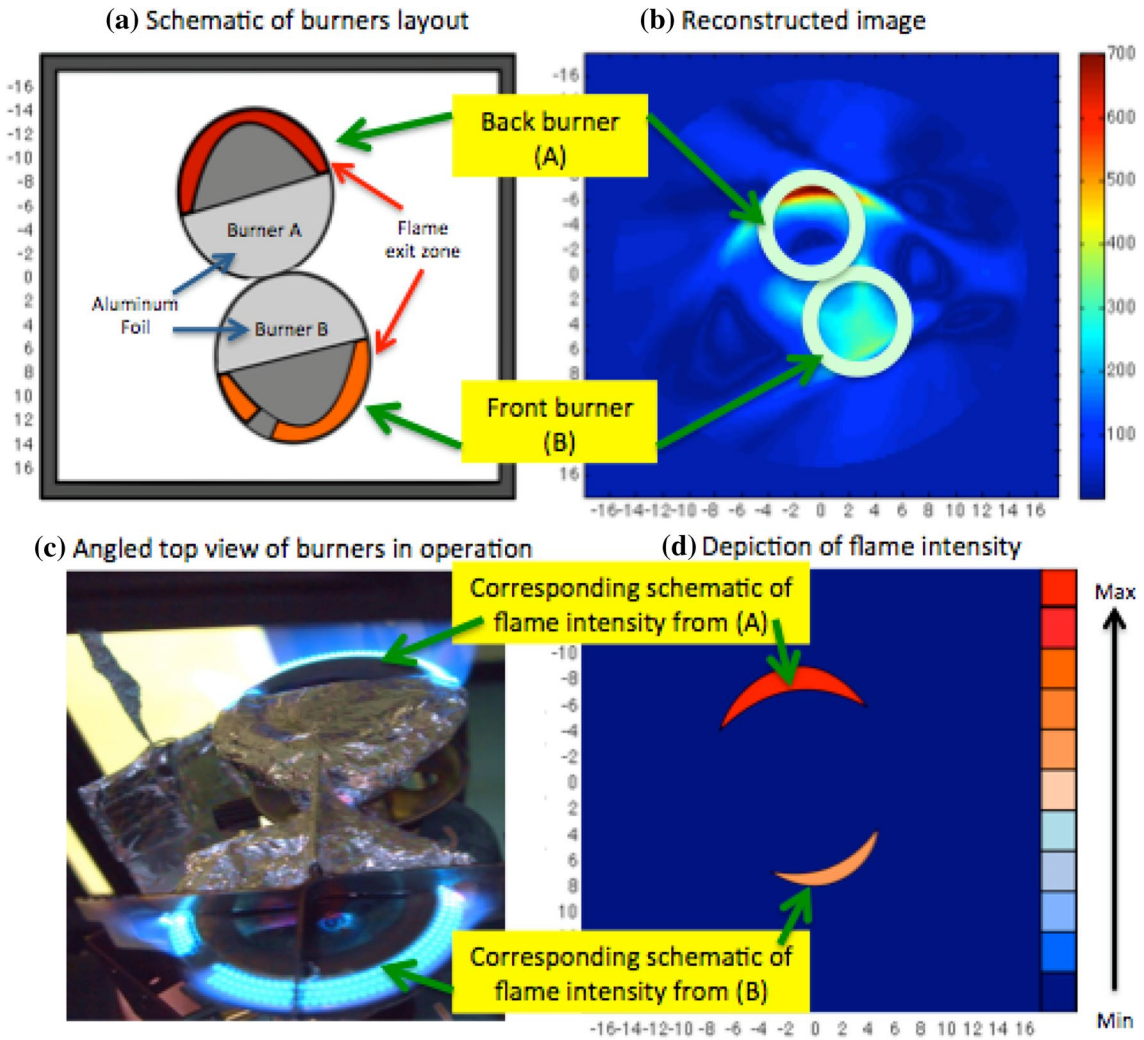

Fig. 15 The correlation between the reconstructed temperature image (**b**) with the schematics (**a**) and photo of flame exit points of the burner (**c**). Burner A is the back burner, while burner B is the front burner. **d** The relative flame intensity

the temperature is extracted (Fig. 14a). With the spatial temperature distributions known, the absorption line strengths and thus concentrations were then determined as shown in Fig. 14b. This method is known as direct Fourier reconstruction (DFR).

3.5 3D and time-dependent experiments

3D measurements were made by taking ten successive 2D sinograms at different heights above the burner with a step size of 1 cm between measurement planes. The 3D experiment was conducted at an ambient temperature of 19.3 °C, an ambient pressure of 101 kPa and a relative humidity of 87%. Time-dependent measurements were conducted by successively measuring the same 2D plane. Each experimental scenario involved adjustment of the fuel flow thus affecting the temperature variation. The experiment was conducted in a series of 16 back-to-back experiments, with a camera installed above the setup to provide a visual pictorial of the actual flame response to gas output manipulation. The time required for a single measurement (sinogram acquisition) to complete, was set at 3.6 s with 360 projections at a 0.5° step size. 16 sinograms were therefore acquired in approximately 1 min (57.6 s). The gas flow was manipulated manually, and additional time was allocated for the user to adjust the fuel gas regulators in between experiments. A total time of 50 s (approximately 3 s per change for 16 settings) was added to the overall experiment run time, raising it to 107.6 s. However, because the time to adjust the fuel was allocated for fuel adjustment, and not the performance of the system itself, it was not added into the results presentation itself as shown.

The time-dependent measurements were conducted at an ambient temperature of 20.4 °C, a pressure of 103.2 kPa and a relative humidity of 79%. The locations of the back burner (A) and the front burner (B) are shown in Fig. 15a where the burners are placed adjacent to each other, with the aluminium foils touching each other creating an asymmetric pattern. An angled top view of the burners in operation is shown in Fig. 15c.

3.6 Validation

Validation of the reconstructed temperature distribution was carried out by thermocouple measurements. It was essential that the thermocouple sampling was undertaken as rapidly as possible to ensure that flame intensity variations did not influence the validation. The thermocouple sensor used for the validation process was Tenma 72-2065A. Its technical specification includes a measuring range between −50 and 1300 °C with an accuracy (non-inclusive of the thermocouple error) of ±0.3% of the final reading +1 °C. A Type K nickel-based thermocouple was used, however the accompanying alloy is unknown, but is usually either chromium or aluminium. The accuracy of this thermocouple is usually between ±2.2 °C and ±0.75%. The thermocouple images were constructed out of 10 × 10 grid cells, acquired on an average of 5 min. The reason for the crude sampling of the thermocouple was because it took too much time to create a denser thermocouple grid. The burner gas output fluctuated over time even at the same opening of the fuel regulator due to the decreasing pressure in the gas canister. The lighter fuel also tends to burn first resulting in a change of fuel composition over time and affecting the intensity of the flame.

The cells were sampled individually using the thermocouple and guides were installed at the top and sides of the external frame to aid accurate placement of the tip of the thermocouple to the correct cells and to distance away from the burner surface. The measurement plane was located 1 cm above the surface of the burner plates.

The thermocouple validation of the DFR shows a close match with the validated maximum temperature spike of reconstructed 705 °C to expected thermocouple readings of 710 °C as shown in Fig. 16. The small temperature

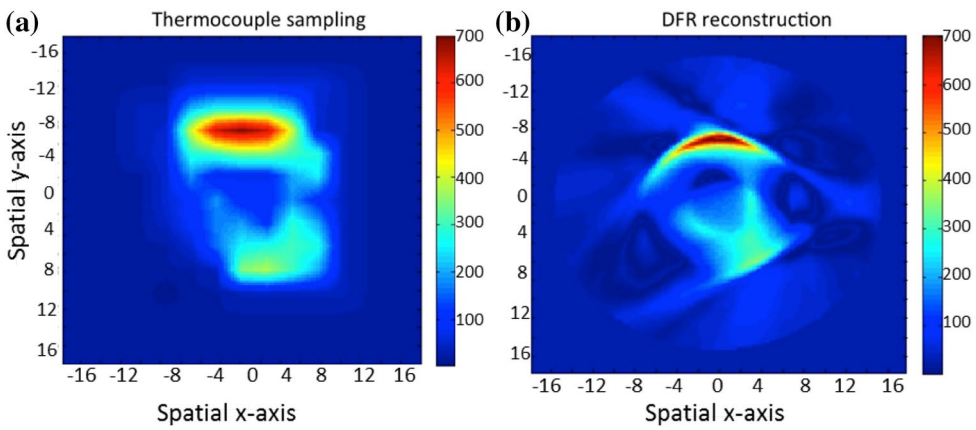

Fig. 16 Comparison of **a** thermocouple sampling of the optical plane with **b** direct Fourier transform reconstruction (DFR) shown in °C

difference may be attributed to a small error in reconstruction as well as a change in temperature output from the burners during the 5 min of thermocouple validation. Because the thermocouple testing had to be executed quickly, some shapes like the curvature of the flame-heating patterns are lost in its representation as shown in Fig. 16.

The comparison of Radon slices of original experimental data and reconstructed by the DFR method yields a close match with the original experimental trends as shown in Fig. 17a. Figure 17b also seems to exhibit minimised flaring and vertical artefacts apparent sometimes in other methods.

4 Results and discussion

4.1 3D reconstructions

The 1 cm-spaced 2D reconstructions at varying height were stacked as shown in Fig. 18. The bottom slice is 1 cm above the burners. View-1 in Fig. 18 shows the ten slices stacked over each other, each slice set at 75% transparency to simulate how it may look as a translucent volumetric space. View-2 in Fig. 18 opens up the slices for an alternative view of each slice. The maximum temperatures from each burner in each slice are marked. As expected, the bottom slice, which is closest to the flame registered the highest

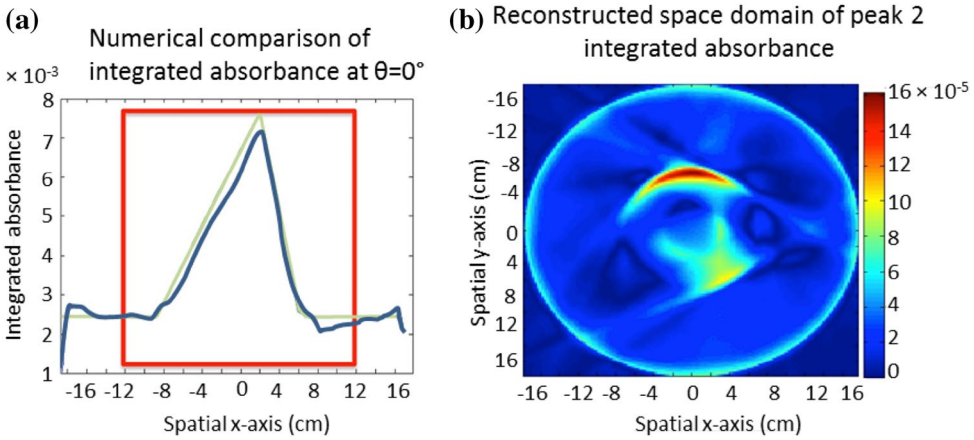

Fig. 17 **a** The numerical comparison of interpolated (*green*) integrated absorbance at radon slice of projection angle 0 with direct Fourier reconstruction method reconstructed (*blue*) integrated absorbance at radon theta 0. **b** The reconstructed integrated absorbance image of peak 2 that was used for the validation process

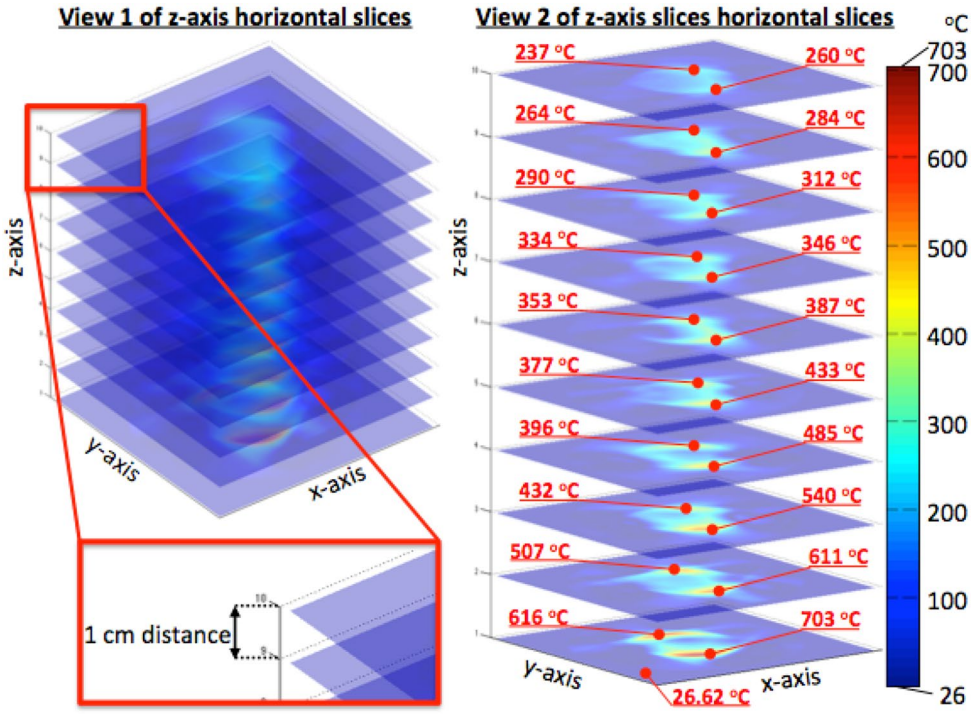

Fig. 18 The individual reconstructed temperature slices vertically spaced 1 cm apart shown in two views. The slice at the *bottom* is the slice closest to the flames, which registers higher temperatures. *View-1* depicts a tighter configuration of 75% transparent slices to simulate a translucent volume. *View-2* shows similar 75% transparent slices that are more spaced out, with the maximum temperatures and locations by the two burners marked out

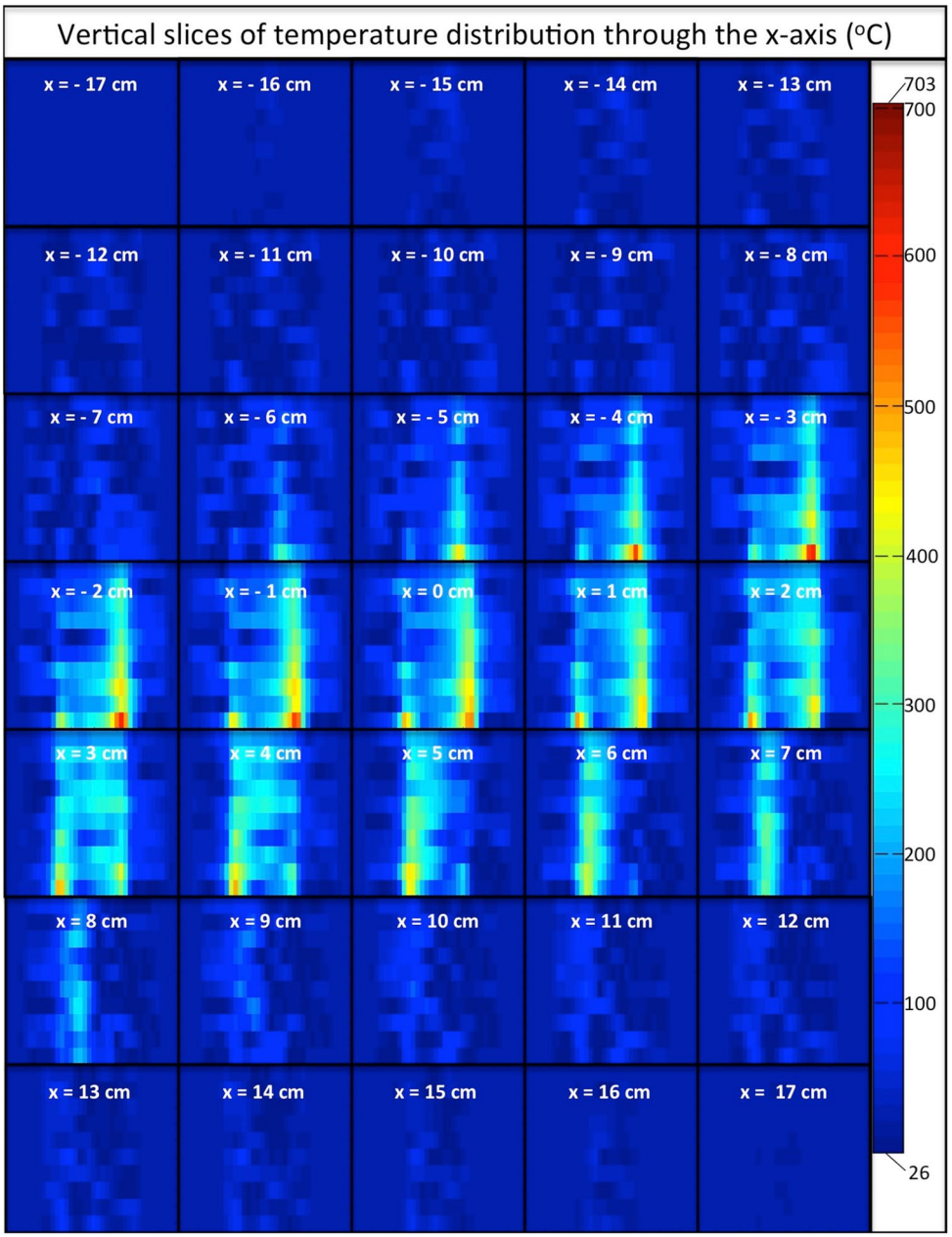

Fig. 19 Individual vertical slices of interpolated temperature with respect to the *x*-axis, from −17 to 17 cm. Note that vertical slice of *x*-axis at −18 and 18 cm were omitted from this figure. Similar constructions were made for the *y*-axis (supplementary data)

temperature and decreases as the slices move further away from the flame.

The gaps between each 2D slice were then linearly interpolated to form a 3D matrix, representing the volumetric space above the burners with dimensions $37 \times 37 \times 10$ cm^3. Vertical slices along both *x*-axis and *y*-axis were then generated from this 3D matrix up to a height of 11 cm above the burners. These vertical slice images were interpolated using MATLAB function 'interp2' and were scaled with a factor of 4 using the "linear" method. Figure 19 represents the full range of the temperature vertical slices along the *x*-axis, from the left to right, *x*-axis (−17 cm) to *x*-axis (17 cm).

It can be observed that the spatial resolution of the vertical slices is poorer (more "pixelated") compared to the horizontal slices shown. This is because the vertical slices are dependent on the spatial resolution of the horizontal slices but also on the number of original horizontal slices as well. The vertical images from both the *x*-axis and *y*-axis are compiled over the base slice to form Fig. 20. A total of 51 slices (vertical axis step size of 0.25 cm) were used from each axis to create a "translucent" volume of spatial temperature distribution.

The two views from both the *x*-axis and the *y*-axis are each presented in Fig. 20. The view from the *x*-axis shows only 1 flame, whilst the *y*-axis shows two flames.

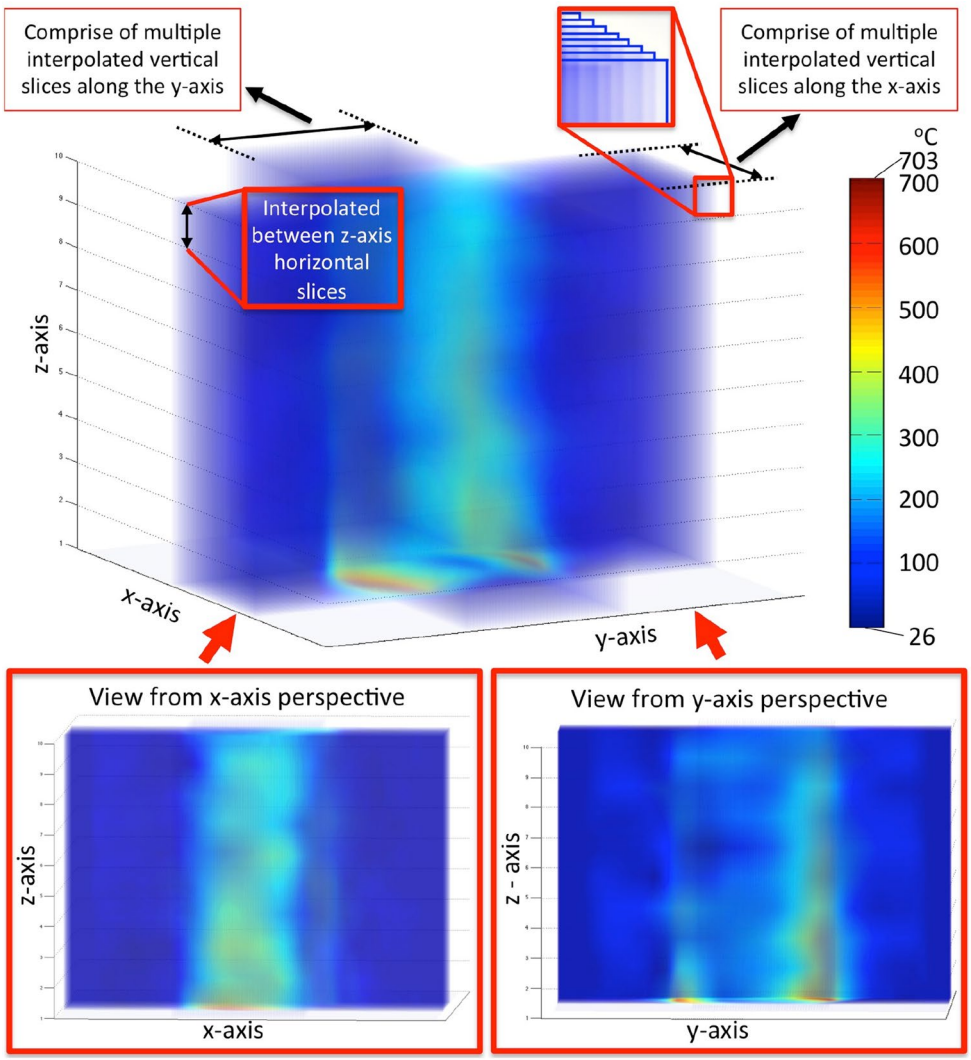

Fig. 20 These are temperature reconstructions. The combined volume is made of 51 slices from the *x*-axis (−25 to 25 cm) and 51 slices from the *y*-axis (−25 to 25 cm). Each slice is set at a transparency of 95% to create a final "translucent" looking volume

4.2 Time-dependent experiments

Figure 21 shows the results of the time-dependent measurements. It took a total of 57.6 s to reconstruct 16 images, which corresponds to 0.28-frame rate per second (fps). The gas regulators of each burner were adjusted based on notches, and the intensity of the each flame is colour coded in the burner schematics in the top rows of Fig. 21. The temporal temperature results are presented underneath the schematic depictions of flame intensities and shown in the bottom rows of Fig. 21. The start time of experiment is 0 s, but the first tomogram could only be generated after the first rotation cycle at 3.6 s. When the regulator notch was tightened, the gas flow decreased and the flame intensity falls and vice versa. The experiment was deemed successful as the temperature reconstructions responded according to the change in fuel regulator gas changes.

The objective of the time-dependent measurements was to use the system as a diagnostic tool to track temperature and concentration changes of a system during operation. This would be particularly useful in terms of monitoring changes in flow or heating patterns across a period of time at a particular section of a pipe, engine or reactor. Ideally, the deployment of lasers sources and detectors should be numerically sufficient to allow the full capture of a full set of projections at different angles without the need for any other form of rotary movements which would allow 'instant' data acquisition. However, an alternative would be to project in a parallel fashion at different angles facilitated by the rotary motor.

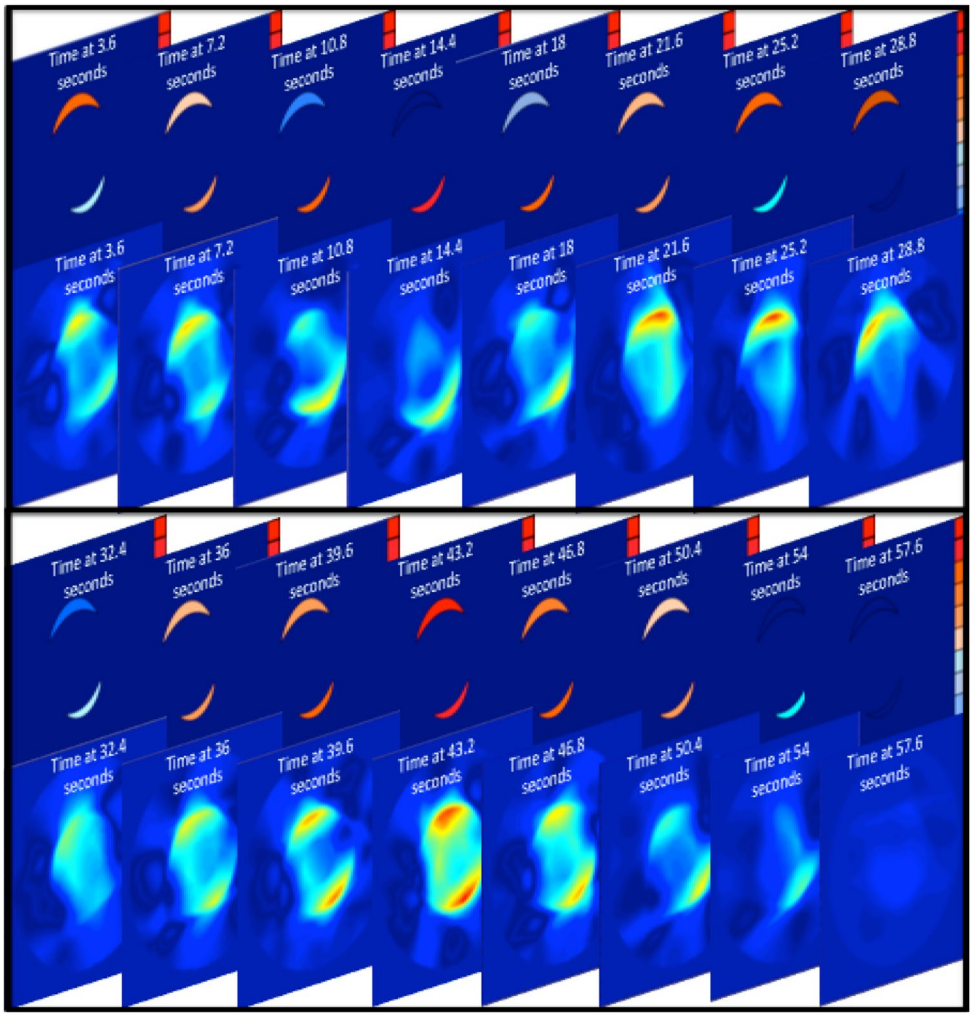

Fig. 21 Reconstructions of temperature distribution with time. The *colour* of each burner in the schematic is indicative of the temperature arising from the change in air/fuel ratio. The increase in shade of *red* indicates increased fuel

5 Discussion

5.1 Pixel resolution

Pixel resolution in general should be balanced between a well-produced image and computational speed/space. A well-produced image consists of image sharpness (where individual pixels could not be seen or that the image should not appear 'blocky') and numerical accuracy of its individual cells. The pixel resolution can only improve as much as its original data allows it to, which means that it is bound to the spatial resolution of that image. If the spatial resolution of the original image is poor, increasing the level of pixel resolution is redundant (consider a film shot in high definition being played on a non-high definition TV). Balancing the pixel resolution with its spatial resolution is important as a high spatial resolution image presented at a low pixel resolution would yield a highly pixelated or 'blocky' image while inversely, a high spatial and pixel resolution would yield a smooth looking image. Figure 22 compares the variation of pixel resolution from 6×6 to 256×256 on a well-sampled image.

From Fig. 22 it is clear that low pixel resolutions from 6×6 to 32×32 not only appear heavily pixelated, but also inaccurate (significantly lower temperature reconstruction by a few hundred degrees celsius). This is because the information present within the high spatial resolution image is averaged into larger cells, thus reducing not only the sharpness but also the numerical accuracy of the image. 64×64 begins to show the correct numerical accuracy of the image but still exhibits pixelated edges. 128×128 exhibits similar smoothness to 256×256 and it can be seen that for the spatial resolution of the original image, a 128×128 pixel resolution representation is sufficient.

5.2 Spatial resolution and number of projections

Spatial resolution is very much determined by the initial data acquisition, and in this tomography system, the data

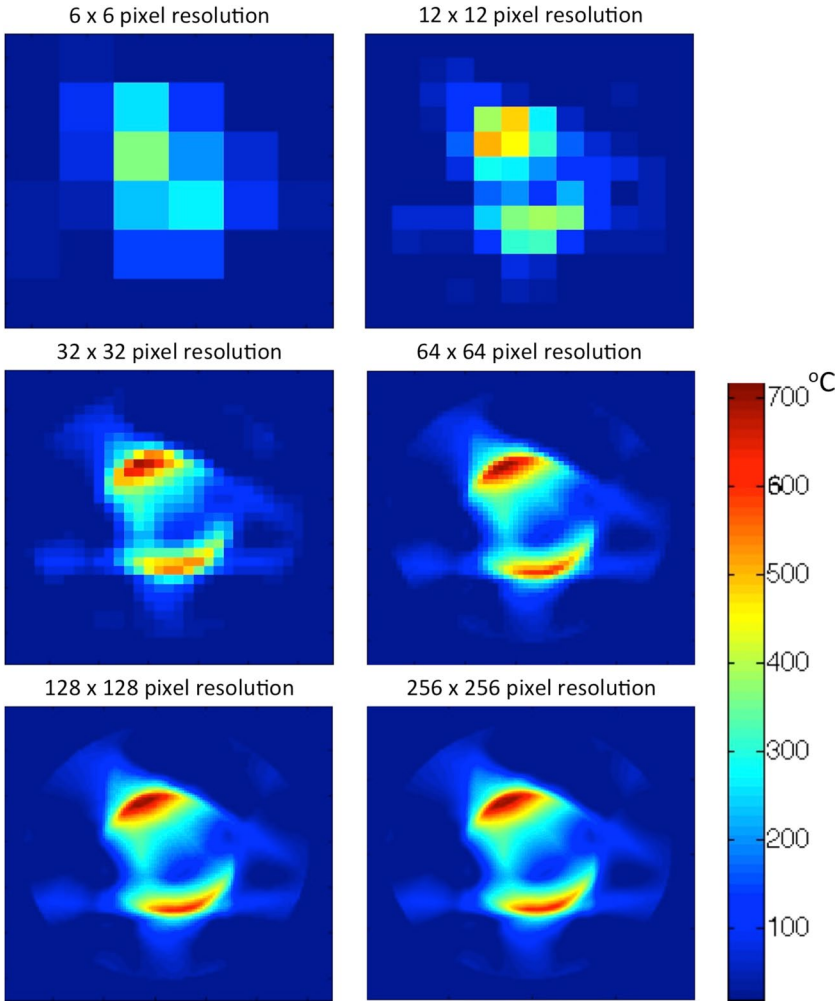

Fig. 22 Variation of pixel resolution to the same image

acquisition is tied to the temporal resolution (maximum/minimum motor speeds) and the desire to minimise the overall experimental time. As such, the only method of increasing the spatial resolution was to increase the number of emitters/detectors per projection angle. The influence of the number of projections on the spatial resolution and numerical accuracy of the temperature distributions was carried out and is shown Fig. 23. 360 projections correspond to an angular step size $\Delta\theta°$ of 0.5° whereas 1 projection corresponds to $\Delta\theta°$ of 180°. These experiments were carried out at an ambient temperatures of 19.3 °C; a pressure of 101 kPa and a relative humidity at 87%. The individual images were produced at pixel resolutions of 128 × 128. Here the main target was to produce a numerically accurate image with the lowest number of projection in the shortest time available.

Using just one or two projections resembles a single or dual back-smearing process of a filtered back-projection (FBP) method. However with only five projections, a rough representation of the correct image can already be observed. From 11 to 45 projections, an image similar to an FBP reconstruction could be observed. These images, due to the lack of projections, resembled a certain degree of blurring on the reconstruction from back-smearing of the data in the FBP process. The temperature values were also substantially suppressed. Most of the streak artefacts in projections from 5 to 45 are no longer present at projection 90. The image has already sharpened significantly and appears to match the visual representation of the flame pattern. However, at this point the temperatures are still not at very accurate. There is not much difference between the reconstructed images of 180–360 projections, yielding similar sharpness. However, at 360 projections, the temperatures are now matching the correct validation values. It can be concluded that a lack of projection data would affect both image quality (blurring) and numerical accuracy. The final image if given the size of 4 cm × 4 cm large, using 360 projections is 81 pixels per inch (PPI).

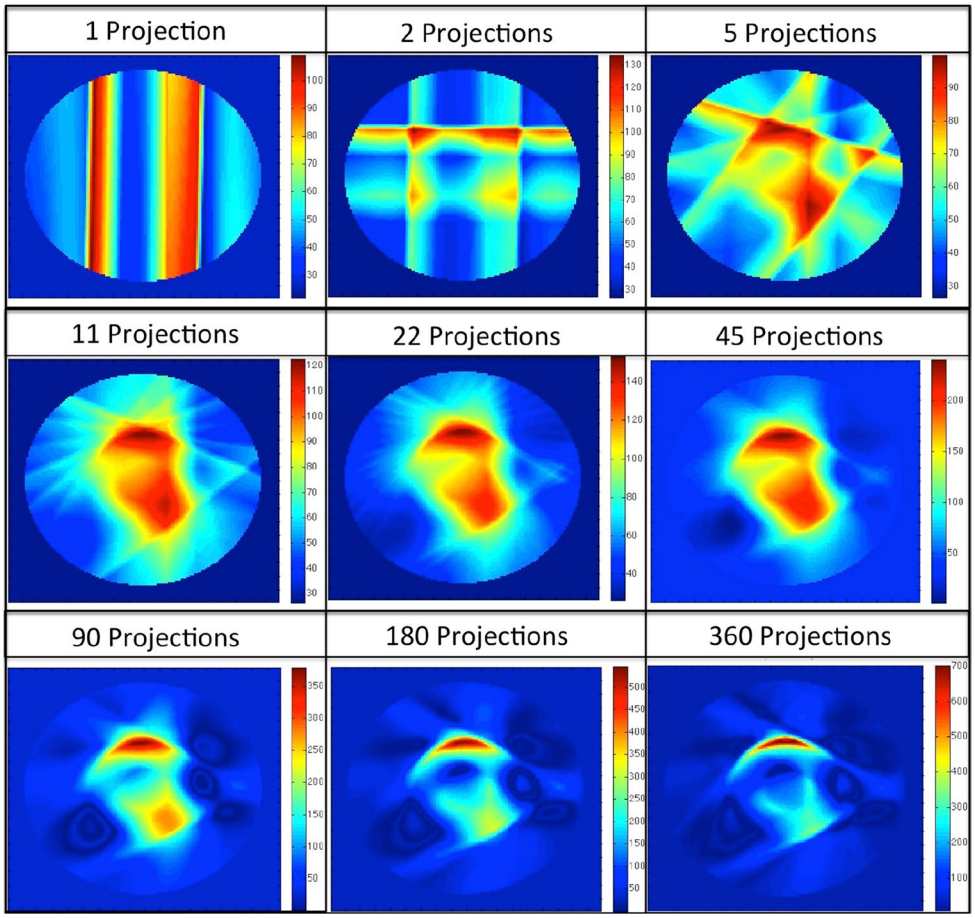

Fig. 23 Resulting reconstructions from variation of step size of the projection angle θ with number of projections

6 Conclusions

In conclusion, a tomographic system has been designed and built for imaging reacting flows in 3D. It uses four parallel laser beams scanning around 1392 nm to probe direct absorption transitions in water produced from an asymmetrical twin burner arrangement. The four parallel beams were rapidly rotated around the object to generate projection data at different observation angles. A reconstruction algorithm based on the FST followed by a 2D ramp filter and inverse Fourier transformation was used to determine firstly the distribution of integrated absorbance for two water transitions and then the temperature distribution by two-line thermometry and finally the water concentration distribution produced from combustion in a 2D plane. Time-dependent measurements of the distributions were demonstrated with a time resolution of 3.6 s (or 0.28 frames per second) as the air/fuel ratio was varied. The burners were moved incrementally to probe successive heights above the burners so that linear interpolation could be made between the ten 2D reconstructed planes to produce a 3D volumetric image of the temperature and chemical species concentrations. However, this is not strictly 3D tomography as only 2D reconstructions are carried out and so it is sometimes called 2.5D. This method provided accurate ± 5 °C reconstructed images with respect to thermocouple validation studies. The pixel resolution of the results were presented in 128×128 pixels and the spatial resolution was recorded using projection intervals at every 0.5°, from 0° to 179.5°, with a total of 360 projections is 81 PPI for a 4×4 cm size image.

There are several approaches that could be taken to improve on the system described here. For example, instead of mechanically raising the object or the optical plane, several optical planes could be sampled simultaneously by fibre-splitting the tunable diode laser beam into further emitter/detector pairs. The laser could be amplified by fibre amplifier systems so that the laser power on each channel is sufficient to avoid detector noise limitations. This would enable temporal 3D measurements to be carried out which were currently only possible in 2D in this work. An alternative would be to use the laser beams with divergent outputs instead of collimated and to use multiple point detectors or array detectors. Probing upwards and downwards through the object would then enable a full 3D tomographic reconstruction without the need to interpolate between slices. The use of array detectors and sheet laser beams would enable denser sampling of the object leading

to a much higher spatial resolution than that obtained here with only four parallel beams [31].

The effects of angular smearing could be reduced by increasing the laser scan rate across the absorption lines. In this case it was limited by the sampling rate of the data acquisition card but faster acquisition is possible. Alternatively, multiplexing fixed wavelength lasers could be used whereby two are employed to monitor the peak amplitude of the two absorption lines used for two-line thermometry and the third is used as a reference to monitor the baseline. However without a wavelength dispersing device the three signals would need to be time-division multiplexed [32]. Measuring multiple species at different wavelengths would also be of great interest. If short tuning range DFB diode lasers are used, as here, then several lasers would have to be multiplexed and scanned in order to detect other species such as CO, CO_2, NO, NO_2 in the flame. The use of supercontinuum lasers has made this much easier with rapid scanning over a wide spectral range [7, 33] but the data quantities generated for tomography may become prohibitive. The detection of species in low concentrations such as free radicals and excited states would be feasible by using cavity-enhanced methods [6] on a stable rotating mount.

The 3D tomography system and result described here demonstrate that such a system can be used for temperature and chemical species concentration distributions in reacting gas flows with applications in combustion systems, plasma reactors and for monitoring stationary or mobile, air pollution.

References

1. C. Schulz, V. Sick, Prog. Energ. Combust. Sci. **31**, 75–121 (2005)
2. S. Roy, J.R. Gord, A.K. Patnaik, P. Taged, Prog. Energ. Combust. Sci. **36**, 280–306 (2010)
3. J. Engstrom, J. Nygren, M. Alden, C.F. Kaminski, Opt. Lett. **25**, 1469–1471 (2000)
4. P.A. Martin, Chem. Soc. Rev. **31**, 201–210 (2002)
5. R.F. Curl, F. Capasso, C. Gmachl, A.A. Kosterev, B. McManus, R. Lewicki, M. Pusharsky, G. Wysocki, F.K. Tittel, Chem. Phys. Let. **487**, 1–18 (2010)
6. G. Berden, R. Engeln, *Cavity Ring-Down Spectroscopy: Techniques and Applications* (Wiley, Chichester, 2009)
7. X. An, T. Kraetschmer, K. Takami, S.T. Sanders, L. Ma, W. Cai, X. Li, S. Roy, J.R. Gord, Appl. Opt. **50**, 29–37 (2011)
8. B. Coriton, A.M. Steinberg, J.H. Frank, Exp. Fluids **55**, 1743 (2014)
9. R.L. Gordon, C. Heeger, A. Dreizler, Appl. Phys. B **96**, 745–748 (2009)
10. J. Nygren, J. Hult, M. Richter, M. Aldén, M. Christensen, A. Hultqvist, B. Johansson, Proc. Combust. Inst. **29**, 679–685 (2002)
11. D. Hoffman, K.U. Münch, A. Leipertz, Opt. Lett. **21**, 525–527 (1996)
12. R.D. Keane, R.J. Adrian, Y. Zhang, Meas. Sci. Technol. **6**, 754–768 (1995)
13. K.Y. Cho, A. Satija, T.L. Pourpoint, S.F. Son, R.P. Lucht, Appl. Opt. **53**, 316–326 (2014)
14. H. Neij, M. Aldén, Appl. Opt. **33** (1994)
15. B.R. Halls, T.J. Heindel, A.L. Kastengren, T.R. Meyer, Int. J. Multiph. Flow **59**, 113–120 (2014)
16. R. Hain, C.J. Kähler, D. Michaelis, Exp. Fluids **45**, 715–724 (2008)
17. W. Cai, C. Kaminski, Prog. Energ. Combust. Sci. **59**, 1–31 (2017)
18. P. Wright, N. Terzija, J.L. Davidson, S. Garcia-Castillo, C. Garcia-Stewart, S. Pegrum, S. Colbourne, P. Turner, S.D. Crossley, T. Litt, S. Murray, K.B. Ozanyan, H. McCann, Chem. Eng. J. **158**, 2–10 (2010)
19. C. Smith, C.S. Goldenstein, R.K. Hanson, Meas. Sci. Technol. **25** (2014)
20. W. Cai, C.F. Kaminski, Appl. Phys. Lett. 104 (2014)
21. M.P. Arroyo, T.P. Birbeck, D.S. Baer, R.K. Hanson, Opt. Lett. **19**, 1091–1093 (1994)
22. X. Liu, X. Zhou, J.B. Jeffries, R.K. Hanson, J. Quant. Spectrosc. Radiat. Transf. **103**, 565–577 (2007)
23. X. Zhou, X. Liu, J.B. Jeffries, R.K. Hanson, Meas. Sci. Technol. **14**, 1459–1468 (2003)
24. V.L. Kasyutich, P.A. Martin, Appl. Phys. B **102**, 149–162 (2011)
25. http://www.hitran.com. Accessed 31 Jan 2017
26. X. Ouyang, P.L. Varghese, Appl. Opt. **29**, 4884–4890 (1990)
27. X. Zhou, J.B. Jeffries, R.K. Hanson, Appl. Phys. B Lasers Opt. **81**, 711–722 (2005)
28. A.C. Kak, M. Slaney, *Principles of Computerized Tomographic Imaging* (IEEE Press, New York, 2001)
29. L.S. Rothman, I.E. Gordon, A. Barbe et al., J. Quant. Spec. Rad. Trans. **110**, 533–572 (2009)
30. http://www.mathworks.com. Accessed 31 Jan 2017
31. M.N.A. tSaoir, D.L.A. Fernandes, J. Sa, M. McMaster, K. Kitagawa, C. Hardacre, F. Aiouache, Chem. Eng. Sci. **66**, 6407–6423 (2011)
32. Y. Gérard, R.J. Holdsworth, P.A. Martin, Appl. Opt. **46**, 3937–3945 (2007)
33. C.F. Kaminski, R.S. Watt, A.D. Elder, J.H. Frank, J. Hult, Appl. Phys. B **92**, 367–378 (2008)